Electrical Machine Loss Distribution and Thermal Parameter Identification through Experimentally Informed Virtual Prototyping

Dominic North*, Suzanne Collins†, Nick Simpson‡ and Phil Mellor§
Electrical Energy Management Group,
University of Bristol,
Bristol, UK
*dn1847@bristol.ac.uk, †suzie.collins@bristol.ac.uk, ‡nick.simpson@bristol.ac.uk, §p.h.mellor@bristol.ac.uk

***Abstract*—Precise loss predictions inform key decisions in the design of high performance electrical machines. Detailed understanding and effective management of operational losses are critical to maximising power density and operational life. Imprecise loss predictions can stem from lack of accurate material and interface data. A method is presented to identify key thermal parameters and AC loss distributions, without construction of a full scale prototype. Using a 3D Virtual Prototype of a machine subassembly, calibrated by experimental data, key parameters such as the conductor-slot thermal conductivity are extracted and implications on machine thermal performance and build quality are inferred.**

***Index Terms*—PM electrical machine, thermal analysis, machine sub-assembly, model calibration, virtual prototype**

I. Introduction

With the increasing trend towards electric vehicles and more-electric aircraft, the demand for more power-dense electrical machines is rising [1], [2]. One barrier to increased power density is dissipation of internally generated heat. Imprecise predictions of intended losses and their distributions can result in over-sized designs to prevent overheating which can negatively impact system power density. Temperature dependent losses exacerbate this problem, hence power dense solutions require coupled electromagnetic and thermal modelling.

Existing thermal modelling methods fall broadly into two groups which compromise between execution speed and accuracy. Lumped Parameter Thermal Networks (LPTN) are commonly used to provide robust, fast calibration of key thermal resistances in machines [3]–[5] but lack fidelity compared to numerical methods such as Finite Element Analysis (FEA) and Computational Fluid Dynamics (CFD). FEA and CFD offer greater resolution and accuracy, but at greater computational cost [5]–[7]. With any method, considerable difficulty still exists when identifying some key thermal parameters, one of which being the thermal conductivity between conductor and stator iron [4], [8]. This interfacing volume, illustrated in Fig. 1, contains mixed materials (slot liner, varnish/epoxy impregnation), air voids, defects and uncertain contact pressures. It is therefore common to model this region as a homogeneous equivalent volume and often to use representative machine subassemblies to define its equivalent thermal parameters empirically [9], [10]. Subassembly testing grants insight into specific machine properties, at reduced time and financial cost, but poorly informed data can still cause significant disagreement between model and production prototype. This is often addressed by costly and time consuming design→build→test iterations.

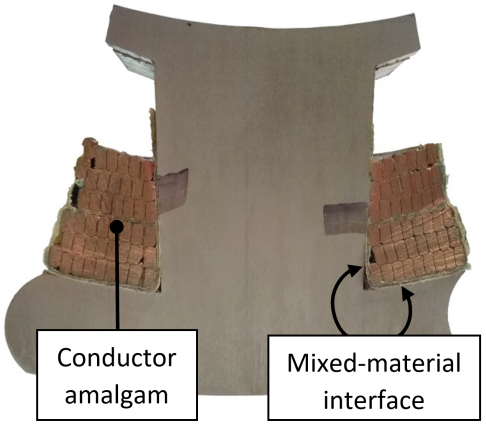

Fig. 1. Example of a mixed-material interface between a conductor and stator tooth. Note voids and imperfect contact.

To reduce the need for such iterations, a simplified method of creating a 3D Virtual Prototype (VP) of the stator winding assembly is presented. The approach has been used to refine and improve the design of a double layer modular wound electrical machine stator, Fig. 2, that employs an open slot winding with preformed, compressed coils. Robust calibration of the VP to experimentally obtained temperature maps from a machine subassembly allows the extraction of important thermal parameters, such as effective thermal conductivity of the winding amalgam and the contact conductance between winding and stator. In addition, the calibrated VP can then be used to obtain detailed information on the magnitude and distribution of AC losses and temperature throughout the winding and core, by comparing virtual and experimental AC loss data. Hence, it is possible to identify problematic loss

(a) Stator representation (b) Motorette

Fig. 2. Computer Aided Design image of double layer modular wound stator investigated and subassembly test prototype of stator winding system manufacture.

concentrations and, with sufficient fidelity, to determine the effect of manufacturing choices on stator losses, e.g. losses at the edges of EDM cut laminations. Significantly, this can be achieved at the design stage.

II. Virtual Prototype Development

The VP is a 3D numerical model capturing the loss and thermal behaviour of the winding coils, with critical thermal and material properties fully defined. It allows 3D analysis of loss distributions as well as providing insight into the effects of manufacturing methods and materials.

To avoid the cost of manufacturing a full stator, a motorette test assembly was used to replicate the winding manufacture and varnish Vacuum Pressure Impregnation (VPI) procedure. The motorette was representative of a 24-tooth, open slot, concentrated-wound, double-layer, permanent magnet machine using multistranded, compressed, aluminium conductors. The conductors were compressed to approximately 70% fill factor, defined as the ratio of aluminium area to the total cross sectional area in the coil active length, where the remainder of the area is made up of strand insulation, varnish impregnation, air voids and any other defects. During construction of the motorette Type K thermocouples were added in key locations to map the temperature distribution within the winding and core, accurate to ±2.5°C, see Fig. 3a where *TC* denotes the thermocouple locations. Thermocouples were also secured to the top surface of the interface plate, adjacent to the motorette iron, and in the ambient air. This motorette did not include a slot closure and thermocouples were inserted into the conductor-tooth and conductor-back iron interfaces, causing small voids between the two. This defect was intended to be identified by the VP as poor thermal conductivity.

For comparison a second motorette was manufactured with two key differences to the first, intended to improve thermal contact between conductor and iron - a difference which should be identified in the VP. The second motorette did not include thermocouples between the winding and iron and had an added slot closure. All other manufacturing processes and materials were identical. The second motorette is shown in Fig. 5, before varnish VPI. An extra thermocouple location

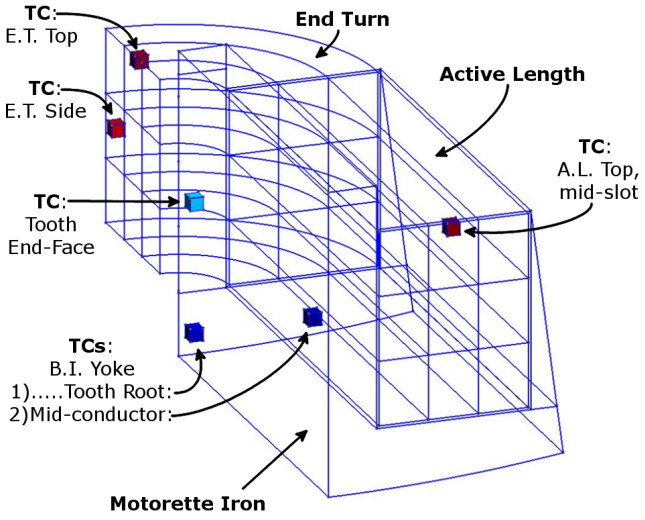

(a) Wireframe model of the VP, representing one symmetric quadrant of the subassembly shown in Fig. 2. *TC* denotes a thermocouple, *A.L.* is the Active Length, *E.T.* the End Turn, and *B.I.* the Back Iron.

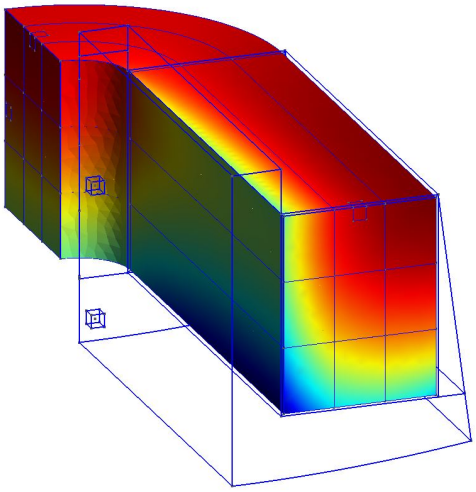

(b) Example temperature map in the conductor of the VP.

Fig. 3. Virtual Prototype: wireframe and example temperature map in the winding region

was added to the second motorette for increased fidelity - labelled "Back Iron Yoke Mid-Conductor" in Fig. 3a.

A 3D numerical model of the winding was formulated, where for computational efficiency thermal symmetry was assumed with only 1/4 of the central tooth modelled. A wire mesh of the model is shown in Fig. 3a where the positions of the thermocouples employed in the test assembly are indicated.

A major focus of the VP is to extract the thermal conductivities of the interfacing regions between the conductor and stator core pack. In the VP these regions have been modelled as equivalent volumes: the mixed-materials and any defects have been combined into a homogeneous, equivalent material with conductivities to represent the amalgam [4], [11], [12]. These volumes are modelled at 0.2 mm thick (≈ slot liner thickness) and contact conductances at their boundaries are considered

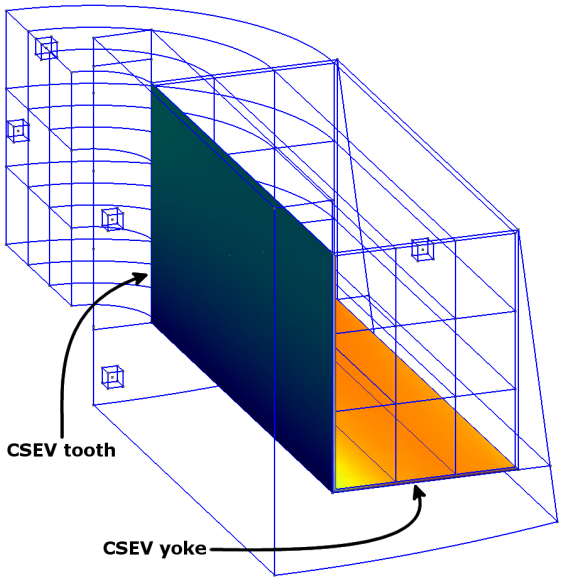

Fig. 4. The Conductor-Stator Equivalent Volume (CSEV) comprising the mixed-material interface between conductor and stator iron.

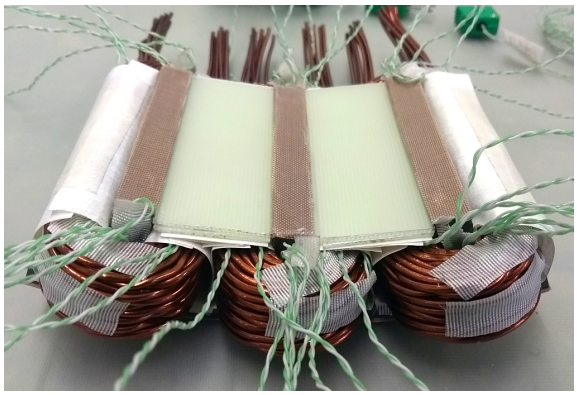

Fig. 5. Three tooth motorette subassembly, including slot closure (not included on first motorette).

perfect. They will be referred to as 'Conductor-Stator Equivalent Volumes' (CSEV) and are visualised in Fig. 4. The thermal behaviour of this conductor-stator interface is highly dependent on materials and manufacture, making it difficult to model [11], [13]. This is particularly true for open slot designs with pre-formed coils because contact pressures are typically lower and less uniform than for coils wound directly onto the teeth. The temperature dependence of electrical resistivity was incorporated by subdividing the conductor volume and defining resistivity as an independent variable in each sub-element, as a function of the local temperature [14]. These subdivisions are visualised in Fig. 3.

Anisotropic material properties (e.g. thermal conductivity) in the VP were defined using datasheet values for bulk or well known materials. For mixed materials' properties (e.g. the winding amalgam) experimentally informed data were used if available [15]. Alternatively, approximations could be

Fig. 6. Cold plate assembly before clamping: motorette, interface plate and water-glycol cooled 6-pass cold plate.

used, such as the Hashin and Shtrikman (H+S) [16] method demonstrated in [9].

An important reference temperature in the VP is at the outer diameter (OD) of the stator iron, which was set constant, as it interfaced to the cold plate apparatus, Fig. 6. The value was determined by extrapolating the back iron yoke temperature to the OD, using its well known thermal conductivity in the lamination plane, and corroborated by the thermocouple measurements on the base plate. To model the AC loss distribution in the VP: the stator model is divided into separate regions (tooth tip, tooth body, and back iron yoke) and the AC loss density will be varied in each local region until agreement with the measured temperature map is achieved.

III. Identification of Thermal Parameters in the VP

An experimental temperature map was established through steady state DC motorette tests, this was repeated with both motorettes. Each motorette was interfaced to a cold plate heatsink and secured using an appropriate clamping apparatus. Thermal contact paste was used at interfaces to ensure homogeneous contact. The motorette and cold plate are shown in Fig. 6. The coil tails were connected in series, noting the current direction in the double layer slots. The assembly was placed in an insulated chamber approximating adiabatic conditions being modelled at the motorette surfaces; the dominant thermal pathway was conduction to the coldplate. Constant DC was injected to the series windings and thermocouple temperatures were logged until thermal steady state was observed. Thermal steady state was defined as less than 1°C change in ten minutes at any thermocouple. DC levels of 25 A, 50 A, and 75 A were used.

FEA was used to compute corresponding virtual maps in the VP. A separate VP was used for each motorette to capture any differences in thermocouple placement. Material parameters were modified in the VPs until the FEA maps agreed with the experimental data. This calibration was performed by a Particle Swarm Optimisation routine (PSO) [17], [18], using Matlab's Global Optimisation Toolbox. The PSO minimised

the objective function shown in (1):

$$f_{obj} = \sum_{i=1}^{m} \left(|T_i^{EXP} - T_i^{FEA}| \right), \quad (1)$$

where m is the total number of thermocouples in the model and T_i is the temperature of the i^{th} one. Superscripts EXP and FEA denote experimental and computed quantities respectively.

The PSO search space was bounded, to ensure solutions could be physically meaningful. Generally, tighter bounds were placed on intrinsic, bulk properties (e.g. resistivity) and less strict bounds were placed on amalgams or materials with uncertain construction (e.g. thermal conductivity across the multistranded conductor bundle).

The PSO was executed multiple times. Each convergence of the PSO produced a unique dataset of thermal conductivities and an objective function result describing how accurately these conductivities reproduced the experimental temperature map in the VP. The objective function results were compared and outliers were discarded if they fell outside +1 standard deviation from the mean. This helped to removed PSO convergences to local minima, which occur because the PSO is a quasi-random process [17], [18]. Across the remaining datasets, the parameters were averaged to yield the final result: a dataset of thermal conductivities for regions in the VP. Finally these values were input to the VP and it was considered calibrated. Crucially, no extensive experimentation or machine construction has been required to gain this information.

The problem is inherently multi-valued, i.e. there may be more than one set of parameters which will converge to a result. To assess the consensus between results, the converged datasets were compiled and the variance of each parameter was computed. A lower variance implied greater consensus in a given parameter's value.

A. Conductor-stator conductivity

The CSEV (see Fig. 4) is a region of special interest; its key parameter being the equivalent thermal conductivity, k_{CSEV} $[W/m.K]$. For comparison the VP was calibrated twice, with isotropic and anisotropic constraints on this parameter. The isotropic condition (CSEV ISO), i.e. $k_{CSEVtooth} = k_{CSEVyoke}$, would decrease calibration time by removing one degree of freedom from the optimisation but sacrifice a layer of fidelity in the model. The anisotropic condition (CSEV ANISO), i.e. $k_{CSEVtooth} \neq k_{CSEVyoke}$, was expected to be more representative of the experimental results by decoupling the two thermal pathways.

IV. Experimental Results and Discussion

Experimental results are presented for the initial (DC) calibrations of the VP, with the four variations discussed in Section III-A (2x motorettes, CSEV ISO/ANISO). Results were averaged from a minimum of fourteen convergences of the PSO in each case, after discarding datasets with outlying objective function results as described in Section III. Thermal conductivities in the calibrated VP are presented in Table I

TABLE I
THERMAL CONDUCTIVITIES IN THE CALIBRATED VP (2 S.F.)

	CSEV ISO.		**CSEV ANISO.**	
VP Region	***M'tte#1*** $k\ \left[\frac{W}{m.K}\right]$	***M'tte#2*** $k\ \left[\frac{W}{m.K}\right]$	***M'tte#1*** $k\ \left[\frac{W}{m.K}\right]$	***M'tte#2*** $k\ \left[\frac{W}{m.K}\right]$
CSEV tooth	0.026	0.047	0.027	0.069
CSEV yoke	0.026	0.047	0.026	0.027
Conductor_{xy}	2.9	2.4	1.9	2.4
Conductor_{z}	170	190	170	190
Iron_{xy}	24	22	22	23
Iron_{z}	0.41	0.36	0.31	0.38

TABLE II
POWER DISSIPATED IN THE CONDUCTOR AT THERMAL STEADY STATE, AT 75ADC.

	CSEV ISO.		**CSEV ANISO.**	
	M'tte#1 [W]	***M'tte#2 [W]***	***M'tte#1 [W]***	***M'tte#2 [W]***
Power Diss. VP	36	29	33	29
Power Diss. EXP	35	32	35	32

where: "M'tte#1" and "M'tte#2" refer to calibration against motorettes 1 and 2 (manufactured with 'poor' and 'good' thermal contact respectively); and the conductivity vectors are isotropic in the planes of the laminations ("Iron_{xy}") and perpendicular to the run of the conductor bundle amalgam ("Conductor_{xy}"). The resultant temperature maps are presented in Fig. 7 as the temperature increase above the back iron tooth root, for each thermocouple location. Computed and experimental power dissipations are compared in Table II and show agreement to within 3 W (10%) in the worst case.

The results given in Fig. 7 show good agreement between key temperatures in the VP and experimental data. The average and maximum absolute errors per probe location are shown in Table III. The temperature differentials in Fig. 7 indicate a significant reduction in winding temperature in the second motorette, which was expected due to the manufacturing differences described in Section II. This is significant as it illustrates the effect of a small manufacturing defect and reinforces the necessity of having robust manufacturing procedures to ensure consistent thermal performance of machines.

The temperature reduction is explained by improved thermal conductivity in the CSEV, as shown in Table I, allowing improved thermal transport away from the loss generating winding. Reduction of temperature during operation is highly beneficial for machine longevity as well as permitting higher operating currents.

The VP has highlighted a significant defect and manufac-

TABLE III
ABSOLUTE TEMPERATURE ERRORS IN THE VP COMPARED TO EXPERIMENTAL TEMPERATURE PROBES.

	CSEV ISO.		**CSEV ANISO.**	
	M'tte#1 [°C]	***M'tte#2 [°C]***	***M'tte#1 [°C]***	***M'tte#2 [°C]***
Average Error	1	1	1	0.4
Max Error	2	3	3	1

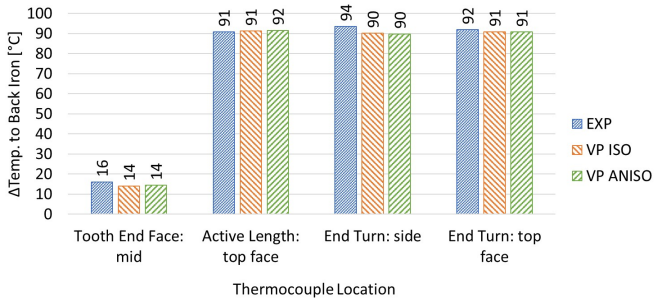

(a) Motorette 1

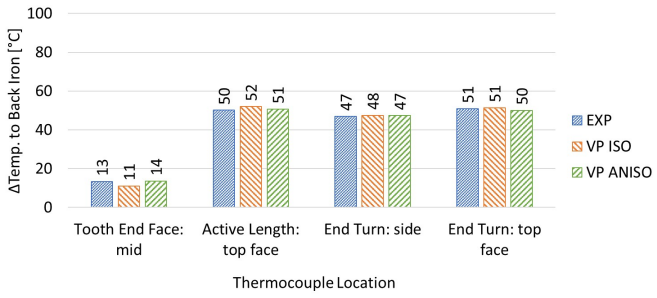

(b) Motorette 2

Fig. 7. Calibrated temperatures in the VP, compared to experimental motorette data (EXP), measured at probe locations shown in Fig. 3a.

turing challenge: thermal contact between pre-formed coils and the stator. Motorette 1 included obstructions between winding and iron and had no slot closure. As predicted the VP computed poor thermal conductivities in the CSEV shown in Table I, for both CSEV ISO and CSEV ANISO calibrations.

Significant air gaps are implied when the results are compared to $k_{air} \approx 0.026\ W/m.K$. In comparison Motorette 2 exhibited improved conductivities in these interfacing volumes, see Table I, owing to improved thermal contact and downward pressure during VPI (removed interface obstructions and added slot closure). It is however noted that in the CSEV ANISO case, Motorette 2 still predicts an air gap in the $k_{CSEVyoke}$ region, compensated by greatly improved conductivity to the tooth side of the conductor in $k_{CSEVtooth}$. Considering the construction methods, slot closure and materials used, a complete air void beneath the conductor is unlikely to be truly representative of the physical reality. It is suspected that the high lateral conductivity in the VP is compensating for a low vertical conductivity out of the conductor bundle.

Reasons for this could lie in the way the optimisation problem was set - if the true global minimum solution was not found there may need to be improvements to the solution parameters or process. Issues could arise in the accuracy and placement of thermocouple probes - providing an incorrect experimental map for the initial calibration, although care was taken in precisely locating the thermocouples to minimise this possibility.

In the case that the VP has correctly identified voids, and there really is an air void between conductor and yoke, further repetitions of this experiment with new motorettes could increase confidence in the result. Further work is planned with more motorettes for this reason.

Regarding the implications on machine construction: poor conductivity between winding and tooth may be attributed to loose fitting concentrated coils due to relaxation or thermal expansion. Wedges could be included in the void between the double layer coils to reduce these effects and further improve thermal conduction to the iron yoke in the mid-slot. It is also important that a properly fitting slot closure is used to maintain downward pressure on the coils during the varnish impregnation procedure.

These results confirm one strength of the proposed VP method - quantifiable validation of manufacturing methods and materials at an early stage. This could allow direct, quantifiable comparison of design variants to ensure the best performance and reduce unknowns at the prototyping stage. It will be desirable to increase confidence in the CSEV ANISO calibration method, to improve the fidelity of the virtual prototype method. This may be necessary for accurate calibration of the AC loss distribution and will be investigated at the experimental and computational stages.

TABLE IV
COMPARISON OF CONDUCTIVITIES IN MOTORETTE 2 CSEV ISO TO A HEAT FLOW EXPERIMENTAL METHOD [19].

	k [W/m.K]		
	Heat Flow	***VP M'tte#1***	***VP M'tte#2***
Conductor_{xy}	2.7	2.9	2.4
CSEV (ISO)	0.031	0.026	0.047

A. Comparing results to other work

The computed thermal conductivity in the CSEV and conductor amalgam can be compared against those from alternative subassembly test procedures. [19] describes the use of an experimental heat flow assembly to directly measure temperatures within a compressed conductor amalgam, then compute its thermal conductivity. [19] used identical materials for the conductor amalgam and bespoke tooling to precompress and subsequently arrange the conductors. During varnish impregnation there was no pressure applied between conductors and 'stator' materials. The conductor packing factor was comparable at 71% (this work: 70%). The work in [19] also computed the thermal conductivity across a representative conductor-stator interface, using identical NOMEX slot liner, and is comparable to the CSER. The comparison between k_{CSEV} in this work is shown in Table IV.

Thermal conductivity across the compressed winding amalgam is comparable between the Heat Flow and VP methods. Table IV shows $k_{Conductor\ xy}$ of the Heat Flow method lying between the two calibrated VP results, to within approximately 10% of either value. This agreement increases confidence in the VP method at this stage in development, although some refinement would be beneficial to increase precision.

The k_{CSEV} results in Table IV can be used to comment on the interfaces in each experimental procedure. The conductor-

stator interface "goodness" can be ranked from worst to best as: Motorette 1, Heat Flow Meter, Motorette 2. This can be observed both in Table IV and from qualitative observations of the experimental manufacture. Motorette 1 contained obstructions between conductor and stator; the Heat Flow Meter arrangement was held uniformly in place, but with no applied pressure; and Motorette 2 used a slot closure and packing to exert some pressure to the interface, in addition to any spring-back from the compressed coil once assembled. Considering these procedures it is reasonable to expect the arrangement of results seen in Table IV and the comparison between experiments reinforces the suitability of the VP for identification of such thermal parameters.

V. Extension to the Present Work: Identification of AC Loss Distribution

The proposed methodology extends to identifying the AC loss distribution using the same motorette and VP. The motorette with 'best' thermal contact was used for this procedure. An experimental AC temperature map was obtained by injecting 1200 Hz (maximum design speed for the considered machine) 75 A_{rms} sinusoidal current into the series connected coils in the motorette. This current level had been previously determined in DC tests not to cause excessive heating in the winding, though machine temperatures were monitored during the experiment to ensure no material thermal limits were exceeded. The same heatsink and insulated chamber were used as in the DC test. Temperatures were monitored and logged until thermal steady state was reached. The corresponding FEA map will be computed in the (now calibrated) VP.

Due to time and equipment availability, the results and analysis of AC data will be reported in a further paper, but the calibration procedure is briefly described here and visualised in Fig. 8. Each model region in the VP will generate heat to simulate AC losses, above the DC losses generated in the winding. The intensity and distribution of AC losses will by varied by PSO until a suitable match to the empirical temperature map is found. The PSO will be repeated until sufficient confidence is seen in the results. The bounds on AC losses will be informed by that measured at the terminals and by electromagnetic modelling.

Given sufficient fidelity, this could reveal important information about AC loss distributions. For instance: at lamination edges (EDM vs. stamped vs. laser cut), for different end winding geometries or for different tooth tip profiles. In addition, modes of degradation could be inferred from calibration with thermally aged motorettes.

VI. Conclusions

The proposed method of creating a Virtual Prototype (VP) of a machine subassembly (motorette) has the potential to reduce financial, material and time costs in the development of electrical machines. 3D FEA has been used to calibrate a VP to experimental data and critical thermal parameters have be extracted for two motorettes exhibiting different manufacturing processes.

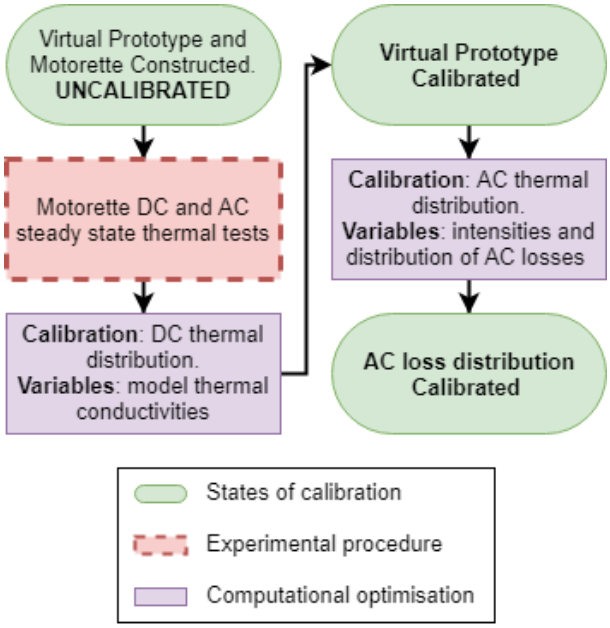

Fig. 8. Virtual prototyping process chart

Manufacturing defects have been identified by the VP. Poor thermal conductivity between winding and stator iron was highlighted in one motorette, implying air voids in the construction. Conductivity was confirmed to be improved in a second VP when better thermal contact was ensured during manufacture. Crucially, the defect was identified at the design stage, before construction of a full machine prototype. In addition, the thermal conductivity of this mixed-material interface was quantified by the VP and could be compared between different assemblies. Some further work is desired to increase confidence when considering increased fidelity in this region, as an anisotropic approach produced unlikely results. In comparison, an isotropic approach has produced more robust results which have been corroborated by results computed in other work. Computed thermal conductivities in the winding amalgam have been computed to a high level of confidence when compared to results from work using another experimental procedure.

The methodology to extend the Virtual Prototyping process and quantify AC loss distributions has been described. Data have been gathered for this purpose and results will be analysed in a further paper.

References

[1] P. Wheeler, "Technology for the more and all electric aircraft of the future," in *2016 IEEE International Conference on Automatica (ICA-ACCA)*, Oct 2016, pp. 1–5.

[2] S. Li, Y. Li, W. Choi, and B. Sarlioglu, "High-speed electric machines: Challenges and design considerations," *IEEE Transactions on Transportation Electrification*, vol. 2, no. 1, pp. 2–13, March 2016.

[3] O. Wallscheid and J. Böcker, "Global identification of a low-order lumped-parameter thermal network for permanent magnet synchronous motors," *IEEE Transactions on Energy Conversion*, vol. 31, no. 1, pp. 354–365, March 2016.

[4] S. Ayat, R. Wrobel, J. Goss, and D. Drury, "Experimental calibration in thermal analysis of pm electrical machines," in *2016 IEEE Energy Conversion Congress and Exposition (ECCE)*, 9 2016, pp. 1–8.

[5] A. Boglietti, M. Cossale, M. Popescu, and D. A. Staton, "Electrical machines thermal model advanced calibration techniques," *IEEE Transactions on Industry Applications*, vol. 55, no. 3, pp. 2620–2628, May 2019.

[6] A. Soualmi, F. Zidat, P. Lombard, and N. Mokhtari, "Thermal study comparison of permanent magnets machines using finite element method (fem) electric vehicles application," in *2018 21st International Conference on Electrical Machines and Systems (ICEMS)*, Oct 2018, pp. 59–64.

[7] S. Nategh, Z. Huang, A. Krings, O. Wallmark, and M. Leksell, "Thermal modelling of directly cooled electric machines using lumped parameter and limited cfd analysis," *IEEE Transactions on Energy Conversion*, vol. 28, no. 4, pp. 979–990, Dec 2013.

[8] A. Boglietti, A. Cavagnino, and D. Staton, "Determination of critical parameters in electrical machine thermal models," *IEEE Transactions on Industry Applications*, vol. 44, no. 4, pp. 1150–1159, July 2008.

[9] N. Simpson, R. Wrobel, and P. H. Mellor, "Estimation of equivalent thermal parameters of impregnated electrical windings," *IEEE Transactions on Industry Applications*, vol. 49, no. 6, pp. 2505–2515, 11 2013.

[10] S. Ayat, R. Wrobel, J. Goss, and D. Drury, "Experiment informed methodology for thermal design of pm machines," in *2016 Eleventh International Conference on Ecological Vehicles and Renewable Energies (EVER)*, April 2016, pp. 1–7.

[11] D. Staton, A. Boglietti, and A. Cavagnino, "Solving the more difficult aspects of electric motor thermal analysis in small and medium size industrial induction motors," *IEEE Transactions on Energy Conversion*, vol. 20, no. 3, pp. 620–628, 9 2005.

[12] R. Wrobel, S. J. Williamson, J. D. Booker, and P. H. Mellor, "Characterizing the in situ thermal behavior of selected electrical machine insulation and impregnation materials," *IEEE Transactions on Industry Applications*, vol. 52, no. 6, pp. 4678–4687, 11 2016.

[13] J. L. Baker, D. Drury, and P. H. Mellor, "Sizing of concentrated-wound permanent-magnet machines using thermal analysis," in *7th IET International Conference on Power Electronics, Machines and Drives (PEMD 2014)*, April 2014, pp. 1–6.

[14] R. Wrobel and N. Simpson, "Winding loss separation in thermal analysis of electromagnetic devices," in *2016 XXII International Conference on Electrical Machines (ICEM)*, Sep. 2016, pp. 2133–2139.

[15] R. Wrobel, N. Simpson, P. H. Mellor, J. Goss, and D. A. Staton, "Design of a brushless pm starter generator for low-cost manufacture and a high-aspect-ratio mechanical space envelope," *IEEE Transactions on Industry Applications*, vol. 53, no. 2, pp. 1038–1048, 3 2017.

[16] Z. Hashin and S. Shtrikman, "A variational approach to the theory of the effective magnetic permeability of multiphase materials," *Journal of Applied Physics*, vol. 33, no. 10, pp. 3125–3131, 1962. [Online]. Available: https://doi.org/10.1063/1.1728579

[17] J. Kennedy and R. Eberhart, "Particle swarm optimization," in *Proceedings of ICNN'95 - International Conference on Neural Networks*, vol. 4, Nov 1995, pp. 1942–1948 vol.4.

[18] J. Robinson and Y. Rahmat-Samii, "Particle swarm optimization in electromagnetics," *IEEE Transactions on Antennas and Propagation*, vol. 52, no. 2, pp. 397–407, Feb 2004.

[19] S. Collins, D. North, P. H. Mellor, and N. Simpson, "Resource efficient determination of electrical machine thermal parameters," in *2019 IEEE Energy Conversion Congress and Expo (ECCE)*, September 2019.